Determinants of target prioritization and regulatory hierarchy for the bacterial small RNA SgrS

Maksym Bobrovskyy[1,2] Jane Frandsen[3,4], Jichuan Zhang[5], Anustup Poddar[5], Muhammad S. Azam[1], Tina M. Henkin[3], Taekjip Ha[5,6] and Carin K. Vanderpool[1]*

[1]Department of Microbiology, University of Illinois at Urbana-Champaign, 601 S. Goodwin Ave., Urbana, Illinois 61801
[2]Present address: Department of Microbiology, The University of Chicago, 920 E. 58th St., Chicago, Illinois 60637
[3]Department of Microbiology and Center for RNA Biology, The Ohio State University, Columbus, Ohio 43210
[4]Biochemistry Program, The Ohio State University
[5]Department of Biophysics and Biophysical Chemistry, Johns Hopkins University, Baltimore, Maryland, USA 21205
[6]Howard Hughes Medical Institute, Baltimore, Maryland, USA 21205

*Corresponding author
Carin K. Vanderpool, Ph.D.
Department of Microbiology
University of Illinois at Urbana-Champaign
C213 CLSL, MC-110
601 S. Goodwin Ave.
Urbana, IL 61801
(t) 217-333-7033
(f) 217-244-6697
cvanderp@life.illinois.edu

Running title: Target prioritization by small RNAs

Abstract word count: 241

Text word count: 6,824

ABSTRACT

The mechanisms by which small RNA (sRNA) regulators select and prioritize target mRNAs remain poorly understood, but serve to promote efficient responses to environmental cues and stresses. We sought to uncover mechanisms establishing regulatory hierarchy for a model sRNA, SgrS, found in enteric bacteria and produced under conditions of metabolic stress when sugar transport and metabolism are unbalanced. SgrS post-transcriptionally controls a nine-gene regulon to restore growth and homeostasis under stress conditions. An in vivo reporter system was used to quantify SgrS-dependent regulation of target genes and established that SgrS exhibits a clear preference for certain targets, and regulates those targets efficiently even at low SgrS levels. Higher SgrS concentrations are required to regulate other targets. The position of particular targets in the regulatory hierarchy is not well-correlated with the predicted thermodynamic stability of SgrS-mRNA interactions or the SgrS-mRNA binding affinity as measured in vitro. Detailed analyses of SgrS interaction with *asd* mRNA demonstrate that SgrS binds cooperatively to two sites and remodels *asd* mRNA secondary structure. SgrS binding at both sites increases the efficiency of *asd* mRNA regulation compared to mutants that have only a single SgrS binding site. Our results suggest that sRNA selection of target mRNAs and regulatory hierarchy are influenced by several molecular features. The sRNA-mRNA interaction, including the number and position of sRNA binding sites on the mRNA and cofactors like the RNA chaperone Hfq seem to tune the efficiency of regulation of specific mRNA targets.

58 **IMPORTANCE**

59 To survive, bacteria must respond rapidly to stress and simultaneously maintain
60 metabolic homeostasis. The small RNA (sRNA) SgrS mediates the response to stress
61 arising from imbalanced sugar transport and metabolism. To coordinate the stress
62 response, SgrS regulates genes involved in sugar uptake and metabolism. Intrinsic
63 properties of sRNAs such as SgrS allow them to regulate extensive networks of genes.
64 To date, sRNA regulation of targets has largely been studied in the context of “one
65 sRNA-one target”, and little is known about coordination of multi-gene regulons and
66 sRNA regulatory network structure. Here, we explore the molecular basis for regulatory
67 hierarchy in sRNA regulons. Our results reveal a complex interplay of factors that
68 influence the outcome of sRNA regulation. The number and location of sRNA binding
69 sites on mRNA targets and the participation of an RNA chaperone dictate prioritized
70 regulation of targets to promote an efficient response to stress.
71

INTRODUCTION

Bacteria live in diverse niches, often encountering rapidly changing and stressful environments. Bacterial stress responses can mitigate the negative effects of stress on cell structure and function. Usually stress responses are coordinated by molecules—either RNAs or proteins, that alter expression of a regulon comprised of multiple genes. Coordinated control of the regulon prepares the cell to survive or adapt to the stress (1, 2). Proteins control expression of target regulons by binding to DNA sequences and modulating the frequency of transcription initiation, but RNAs often modulate gene expression post-transcriptionally. A prevalent type of RNA regulator in bacteria is referred to simply as small RNA (sRNA). These sRNAs are often produced in response to a particular stress, and regulate target mRNAs through base pairing interactions that modify mRNA translation or stability (3, 4). In diverse bacteria, hundreds of sRNAs have been identified (5-7). While the majority of sRNAs have not been characterized, many studies suggest that sRNA regulatory networks are as extensive and complex as those controlled by proteins (8, 9).

A large body of work has illuminated base pairing-dependent molecular mechanisms of post-transcriptional regulation by sRNAs (10, 11). The sRNA SgrS (sugar-phosphate stress sRNA) has been an important model for discovery of both negative and positive mechanisms of target mRNA regulation. SgrS is induced in response to metabolic stress associated with disruption of glycolytic flux and intracellular accumulation of sugar phosphates (also referred to as glucose-phosphate stress) (12, 13). SgrS regulates at least 9 genes and promotes recovery from glucose-phosphate stress. SgrS-dependent repression of mRNAs encoding sugar transporters

(*ptsG, manXYZ*) reduces uptake of sugars to prevent further sugar-phosphate accumulation (Fig. 1) (12, 14, 15). Activation of a sugar phosphatase (*yigL*) mRNA promotes dephosphorylation and efflux of accumulated sugars (16), and repression of other mRNAs is hypothesized to reroute metabolism to promote recovery from stress (Fig. 1) (17). Each target of SgrS is regulated by a distinct molecular mechanism. How different mechanisms of regulation yield effects of variable magnitude with respect to mRNA stability and translation is an open question.

Temporally-ordered and hierarchical patterns of gene regulation carried out by protein transcription factors have been characterized in many systems (18-21). These regulatory patterns allow cells to efficiently respond to environmental signals by prioritizing induction or repression of products needed to respond to those signals. Protein regulators establish a hierarchy of regulation based on their affinities for binding sites in the operator regions of different target genes. As the concentration of active regulator increases, genes are sequentially regulated based on binding site affinity (22). There is growing evidence that sRNAs also regulate their target genes hierarchically (23, 24). However, the mechanisms involved in establishing and maintaining prioritized regulation of sRNA targets are not known.

We hypothesize that the temporal progression of target regulation by SgrS is specifically optimized to promote efficient recovery from glucose-phosphate stress (Fig. 1). To test this hypothesis, first defined the efficiency of SgrS regulation of each target and found that SgrS indeed prioritizes regulation of some targets over others. We examined the factors that determine regulatory efficiency, including the the arrangement and strength of SgrS target binding sites and the roles of other factors like RNase E and

Hfq. Detailed characterization of a specific SgrS-mRNA target interaction revealed cooperative binding of SgrS to two binding sites and a requirement for both binding sites for maximal SgrS-dependent regulation. Collectively, our results upheld the hypothesis that sRNAs regulate expression of genes in their target regulons hierarchically. Features of each sRNA-mRNA pair and molecular mechanisms of regulation precisely determine the regulatory priority for each target.

RESULTS

SgrS differentially regulates targets at the level of translation. Previous studies suggested the possibility of a hierarchy of regulatory effects carried out by the small RNA SgrS, which controls translation of a diverse set of mRNA targets (11, 12, 15, 16, 25). To study this, we used a two-plasmid system to control expression of SgrS and target translational fusions (Fig. 2A). All target transcript fragments fused to *gfp* contain experimentally confirmed SgrS binding sites. Regulation of target translation by SgrS was measured as described previously (24).

To quantify translational regulation by SgrS and facilitate comparisons of regulatory efficiency among targets, we analyzed the data as described by Levine, et al. (24). Activity of reporter fusions was measured by monitoring GFP fluorescence over time. By plotting the GFP fluorescence (RFU) as a function of growth (OD_{600}) for target-*gfp* fusions in the absence of SgrS, we defined “basal activity” at different inducer concentrations (example in Fig. S1A). This method of quantifying translational fusion activity accounts for the fact that fluorescence levels are not directly proportional to inducer concentrations ((24) and Fig. S1A). While the absolute values for basal activity differ among different target fusions, all fusions responded to induction in a dose-

dependent manner (Fig. S2A). Similar plots (RFU/OD_{600}) were generated for each fusion induced in the presence of SgrS (examples Fig. S1B-F). We define "regulated activity" as the slope of the curve (RFU/OD_{600}) under conditions where both the fusion and SgrS are induced (example in Fig. S1B). As levels of SgrS increase, clear patterns of repression or induction are seen for all target fusions (Figs S1B-F and S2B-F).

To define the efficiency of regulation of each target we plotted regulated activity as a function of basal activity for *ptsG*, *manX, asdI, purR,* and *yigL*. When there is no SgrS-mediated regulation, a line with a slope of 1 is seen for all targets (Fig. 2B-F). Slopes less than 1 indicate that the fusion is repressed by SgrS. This is true for *ptsG*, *manX*, *asdI* and *purR* reporter fusions (Figure 2B-E). Slopes greater than 1 are indicative of activation by SgrS, which is true only for *yigL* (Fig. 2F). Importantly, the magnitude of regulation was responsive to SgrS levels. As concentrations of SgrS inducer (aTc) increased, slopes of lines for repressed targets were correspondingly reduced (Fig. 2B-E). This was not the case for *yigL,* the only positively regulated target of SgrS (Fig. 2F). The magnitude of activation did not increase beyond a maximal level obtained at 20 ng/mL of inducer. While the basis of this difference is unclear, it likely reflects the inherently different molecular mechanisms of regulation: mRNA stabilization for *yigL* and translational repression for all other targets.

We then compared regulatory efficiency among different targets at different levels of SgrS induction. At the two lowest levels of SgrS induction (10ng/mL and 20 ng/mL aTc), only *ptsG* and *yigL* showed substantial repression and activation, respectively (Fig. 3A, B). In contrast, *manX*, *asdI* and *purR* fusions yielded curves whose slopes remained at ~1, indicating no regulation at these lower levels of SgrS.

Our interpretation of these results is that *ptsG* and *yigL* are the high-priority or "strongest" targets of SgrS, since they are regulated preferentially when SgrS levels are low. With increasing SgrS levels (20-50 ng/ml aTc), regulation of "weaker" targets *manX, asdI* and *purR* became apparent (Fig. 3C, D, E). As SgrS levels increased, *ptsG* repression became more efficient up to a maximal repression at 40 ng/mL of aTc, and it remained the most strongly repressed target at all levels of SgrS. Collectively, these data suggest that SgrS targets are preferentially regulated in the following order: 1/2) *ptsG* and *yigL*, 3) *manX,* 4) *asdI*, and 5) *purR* (Fig. 3A-E). We hypothesize that the position of each target within the regulatory hierarchy is determined by characteristics of SgrS-target mRNA interactions and the mechanism of SgrS-dependent regulation.

Differences in in vitro binding affinity are not correlated with regulation efficiency. One of the initial steps in sRNA-mediated regulation is formation of base-pairing interactions with the target mRNA. Binding of the sRNA with its target mRNA is dependent on sequence complementarity and RNA secondary structure. We examined the characteristics of SgrS-target mRNA binding in vitro to determine whether the strength of binding is correlated with the target hierarchy observed at the level of translation.

Electrophoretic mobility shift assays (EMSAs) were performed to measuring binding of SgrS to its target mRNAs *ptsG*, *manX*, *purR*, *yigL* and *asd*. Binding of SgrS to *ptsG* had *a* K_D of 0.11 ± 0.01 µM (Fig. 4A, B), which was lower than K_Ds for SgrS binding to most of the other targets (Fig. 4A-E). SgrS-*manX* mRNA binding had a K_D of 19.7 ± 2.78 µM (Fig. 4A, C) which is weaker than the interaction with *ptsG* (Fig. 4B), but stronger compared to *purR* and *yigL* (Fig. 4A). Three different fragments of *asd* mRNA

were tested, because previous work demonstrated that SgrS pairs at two distinct sites on *asd* mRNA (17). The first site, *asdI*, is adjacent to the ribosome binding site and is sufficient for modest SgrS-dependent translational repression. The second site, *asdII,* is in the coding sequence of *asd,* 60-nt downstream of the start codon. When both sites are present, *i.e.,* on *asdI-II,* stronger SgrS-dependent translational repression is observed (17). Surprisingly, while *asdI* (containing only the upstream SgrS binding site) regulation is less efficient compared to *manX* (Fig. 3A-E), *in vitro* it binds SgrS more strongly with a K_D of 0.15 ± 0.04 µM (Fig. 4A, D), which is comparable to SgrS-*ptsG* binding (Fig. 4A, B). SgrS interaction with *asdII* was very weak (Fig. 4A). We could not determine K_D values for SgrS interaction with *asdII*, *purR* and *yigL*, due to limitations in obtaining high enough concentrations of RNA, but it is apparent that SgrS binding to these targets is much weaker compared to *ptsG*, *manX* and *asdI* (Fig. 4A).

Results of EMSAs with SgrS and *asdI-II* (containing both SgrS binding sites) revealed apparent binding cooperativity. SgrS binding to *asdI-II* has a K_D of 0.07 ± 0.01 µM (Fig. 4E, F), even slightly lower than that of SgrS-*ptsG* mRNA binding. Moreover, we observed two shifted species that correspond to one or two SgrS sRNAs pairing with a single *asdI-II* transcript (Fig. 4E).

Structural analyses of SgrS-*asd* mRNA interactions. Our data thus far indicate that SgrS regulates mRNA targets in a hierarchical fashion (Figs. 2, 3). SgrS-mRNA binding affinities alone do not explain the target hierarchy, as SgrS-*ptsG* mRNA and SgrS-*asd* mRNA interactions have very similar K_Ds, but *ptsG* is much more efficiently regulated than *asd* at all concentrations of SgrS (Fig. 3). To further understand the features that

influence the efficiency of target regulation, we performed more detailed analyses of SgrS-*asd* mRNA interactions.

Previous work demonstrated that SgrS binding site I encompasses nt +31 to +49 and site II from nt +110 to +127 ((17), Fig. 5A) We used IntaRNA (26, 27) to predict the free energy (ΔG) for SgrS interactions with *asd* mRNA segments containing both sites, or each site individually (Fig. 5B). IntaRNA accounts for the energy necessary to open double-stranded regions of RNA secondary structure, to make them accessible for pairing. We first analyzed SgrS interactions with *asdI-II* mRNA (encompassing nt +1 to +240), which we denote as “structured” (Fig. 5B). Interaction of SgrS with *asd* site I has a predicted ΔG of -10.5 kcal/mol, while SgrS pairing with site II has a ΔG of -1.1 kcal/mol (Fig. 5B, structured). The ΔG for interactions between SgrS and the isolated binding sites, are -18 kcal/mol for site I and -7.4 kcal/mol for site II (Fig. 5B, isolated). These predictions suggest that SgrS interaction with site II is less favorable, particularly in the context of the longer structured *asd* mRNA.

We investigated the structure of *asdI-II* with selective 2'-hydroxyl acylation analyzed by primer extension (SHAPE), where flexible nts are modified by N-methylisotoic anhydride (NMIA), while nts constrained in helices are not reactive. In the absence of SgrS, the sequence encompassing the *asd* ribosome binding site (+44 to +50) is located within a structured loop (+36 to +69) on top of a short stem (+31 to +35 pairing with +70 to +74) (Fig. 5C, Fig. S3). The nts in site I (+31 to +49, Fig. 5A) are located on the 5’ side of the stem-loop structure. Most of the nts in this structure are reactive, which is indicative of a flexible conformation that is accessible for ribosome binding or base pairing with the seed sequence of SgrS (Fig. 5C). The seed interaction

of SgrS likely promotes opening of the structure. Downstream of the site I stem-loop structure is a highly structured second stem (+83 to +155) that contains site II in the apical region (+110 to +129) (Fig. 5C, Fig. S3). Site II is sequestered in a helix and would not be accessible to base pair with SgrS (Fig. 5C). In light of binding cooperativity observed in Fig. 4E, we hypothesize that SgrS pairing with site I induces rearrangement of *asd* mRNA secondary structure to facilitate interaction with site II.

We next used SHAPE to probe changes to the *asdI-II* structure in the presence of SgrS. The reactivity of site I nt +31 to +49 decreased as the concentration of SgrS increased (Fig. 5D), with the exception of nt +41 which is not predicted to base pair with SgrS (Fig. 5A). The SHAPE reactivity plateaued between 5 and 10-fold excess SgrS (Fig. S3E,F), which suggests that binding to site I was saturated. This is consistent with a strong base-paring interaction between SgrS and site I. In contrast, the reactivity of the site II nts +110 to +129 decreased more slowly and to a lesser extent (Fig. 5D), consistent with a weaker and cooperative interaction. Fewer site II nts showed changes in SHAPE reactivity upon addition of SgrS; this is likely due to the highly structured nature of site II in the absence of SgrS.

The reactivity of nts outside of the SgrS binding sites also changed in the presence of SgrS (Fig. 5E). When a mutant SgrS that is not predicted to bind to *asdI-II* was used, minimal changes in SHAPE reactivity were observed, which suggests that the changes in the presence of wild-type SgrS are due to the interactions between SgrS and *asdI-II* mRNA and not due to the presence of additional RNA in the system (Fig. 5E). This indicates that SgrS binding changes the overall structure of the *asd* RNA. A secondary structure predicted using the SHAPE data suggests that these changes are

limited to opening the SgrS binding sites and extending the site II stem (Fig. 5C). It is worth noting an important caveat to these analyses. The structure prediction algorithms were not designed to account for intermolecular interactions, so this analysis may not be able to capture the in vivo relevant structure of *asd* mRNA in complex with SgrS. Nonetheless, SHAPE data are consistent with other analyses in demonstrating binding of SgrS to *asd* mRNA, prominently at site I and to a lesser extent at site II.

Optimal repression by SgrS involves both pairing sites within *asd* mRNA. To further investigate the role of the two SgrS pairing sites on *asd*, we performed stochastic optical reconstruction microscopy (STORM) coupled with single-molecule *in situ* hybridization (smFISH) to monitor SgrS regulation of *asd-lacZ* variants *asdI, asdII,* and *asdI-II* (Fig. 6A) at single molecule resolution. In these experiments bacteria were grown in the presence of L-arabinose to induce expression of chromosomal *asd-lacZ* variants. Glucose-phosphate stress was induced for 10 min by the addition of 1% α-methyl D-glucopyranoside (αMG). 3D super-resolution images show *asd-lacZ* mRNAs (Fig. 6B-D, green) and SgrS (Fig. 6B-D, red), as projected on 2D planes, with cells outlined. Numbers of *asd-lacZ* mRNAs and SgrS sRNAs were counted and represented as “copy number per cell” in histograms, with average copy number per cell indicated above the histogram (Fig. 6B-D). SgrS induction reduced the copy number of *asdI-lacZ* mRNA by 3-fold (Fig. 6B, green) when SgrS was induced to high levels after 10 min treatment with αMG (Fig. 6B, red and S4A, B). On the contrary, the copy number of *asdII-lacZ* mRNAs (Fig. 6C, green) was not strongly affected in the presence of high SgrS levels after αMG treatment (Fig. 6C, red and Fig. S4C, D). Copy numbers of *asdI-II-lacZ* mRNA (Fig. 6D, green) were reduced by ~8-fold after 10 min of αMG induction (Fig. 6D, red, Fig.

278 S6E,F). These data demonstrate that both binding sites on *asd* mRNA are important for
279 efficient SgrS-dependent regulation of mRNA stability.

280 We next examined the roles of the two SgrS binding sites in the efficiency of
281 translational regulation. SgrS regulation of an *asdI-II* translational fusion was compared
282 to regulation of an *asdI* fusion (Fig. 7A). By plotting regulated activity as a function of
283 basal activity as described above, we determined that SgrS repression of *asdI-II* was
284 more efficient than repression of *asdI* across the entire range of SgrS expression levels
285 (Fig. 7B), a result in line with our previous study (17). Comparison to other targets
286 indicated that *asdI-II* is regulated more efficiently than *manX*, *asdI* and *purR*, at all
287 concentrations of SgrS (Fig. 7C).

288 We then compared SgrS regulation of *asdI* and *asdI-II* in the *rne701* mutant
289 strain deficient in degradosome assembly (28). We determined basal activity (Fig. S5A)
290 and regulated activity (Fig. S5B-F) of *asdI* and *asdI-II* translational *gfp* fusions at
291 different levels of SgrS induction. Reminiscent of our data in the wild-type strain (Fig.
292 7A), SgrS regulated *asdI-II* more efficiently compared to *asdI* in the *rne701* mutant (Fig.
293 7D. Moreover, when compared to SgrS regulation of other targets, *asdI-II* was
294 repressed most efficiently (Fig. 7E) in the *rne701* mutant. Taken together the data
295 indicate that the second binding site on *asd* mRNA enhances the stringency of SgrS-
296 mediated regulation. Moreover, addition of the second binding site on *asd* changes its
297 regulatory priority relative to other targets in the SgrS regulon.

298 **Transcriptional regulation of *asd* by SgrS.** We observed that the *asdI-II* transcript is
299 more abundant than *asdI* (Fig. 6B, D). Since the constructs used in that experiment
300 were expressed from a heterologous promoter, we postulate that increased levels of

asdI-II mRNA compared to *asdI* mRNA must be due to increased mRNA stability or transcription elongation of the *asdI-II* construct compared to *asdI.* We constructed *asdI* and *asdI-II* transcriptional fusions to *lacZ* expressed from an inducible promoter (Fig. 8A) to test whether SgrS can regulate *asd* transcripts independent of translational regulation. Consistent with observations from smFISH, the *asdI-II-lacZ* transcriptional fusion had substantially higher activity compared to *asdI-lacZ* (Fig. 8B). While SgrS regulated both reporter fusions, *asdI-II* repression was more efficient (3.3-fold repression) than *asdI* (2.1-fold repression) (Fig. 8B). SgrS still regulated both fusions in the *rne701* mutant strain (Fig. 8B). Importantly, SgrS-dependent degradation of other SgrS targets *ptsG* mRNA (29), and *manXYZ* mRNA (15, 25) was abolished in degradosome mutants. Together with our previous work, these observations suggest that SgrS regulates *asd* by two independent mechanisms: translational repression by pairing at site I (directly occluding the ribosome binding site) and reducing mRNA levels by promoting mRNA turnover and/or inhibiting transcription elongation.

DISCUSSION

In this study, we set out to define the hierarchy of regulation by a model bacterial sRNA. SgrS is a good model for this study because it has a modestly-sized regulon, and the mechanisms of regulation of several targets have been characterized in detail (16, 17, 25, 30). Our results demonstrate a clear pattern of prioritized regulation of mRNA targets (Fig. 2B-F, Fig. 3A-E). Two targets in particular, *ptsG* and *yigL,* were “high-priority” targets that were efficiently regulated even at low levels of SgrS production. Other targets, *manX, purR,* and *asd,* were less impacted by SgrS and were only regulated when SgrS was produced at higher levels.

We investigated features of sRNA-mRNA interactions that could impact the overall efficiency of SgrS-mediated regulation. In vitro SgrS-mRNA interactions as measured by EMSA defined K_Ds that were not well-correlated with in vivo regulatory efficiency (Fig. 4A-F, Fig. 3A-E). Two targets stood out in the comparison of in vivo regulation and in vitro SgrS-mRNA interactions. The *yigL* mRNA interaction with SgrS was barely detectable in vitro (Fig. 4A), but in vivo, *yigL* translation was maximally activated at low SgrS levels (Fig. 2F). Conversely, the translation of *asdI* was modestly regulated by SgrS in vivo (Fig. 2E), but the in vitro SgrS-*asdI* interaction was comparable to that of SgrS-*ptsG,* the strongest in vivo regulatory effect. These apparent contradictions between in vitro interactions and in vivo regulatory efficiency led us to further explore SgrS regulation of *asd.*

Previous work demonstrated that SgrS has two binding sites on *asd* mRNA: site I overlaps that *asd* ribosome binding site and site II is ~60 nt downstream in the *asd* coding sequence ((17) and Fig. 5A). EMSAs demonstrated SgrS pairing at site I alone, but pairing at site II alone was undetectable. Binding of SgrS to an *asd* mRNA containing both sites I and II was cooperative (Fig. 4E,F). Structural analyses of *asd* mRNA in the absence and presence of SgrS demonstrated that SgrS indeed pairs preferentially at site I over site II and induces substantial structural rearrangement in the mRNA (Fig. 5C-E, Fig. S3). Quantification of SgrS-dependent degradation of *asd* mRNA showed that site I is important, but sites I and II together promote the most efficient regulation (Fig. 6B-D, Fig. S4). Similar to binding and regulation of mRNA degradation, SgrS interactions at both sites I and II on *asd* mRNA improve the efficiency of translational regulation (Fig. 7B,C, Fig. S2). These results suggest that the number and

position of sRNA binding sites on mRNA targets control regulation in vivo in ways that could not be predicted based on in vitro characterization of sRNA-mRNA binding.

In many cases, sRNA-mediated regulation of translation is thought to indirectly affect mRNA stability by making untranslated mRNA more susceptible to degradation by RNase E. There are also examples of sRNA regulation, including SgrS regulation of *yigL* (16), where modulation of mRNA stability is translation-independent. Truncation of RNase E (encoded by *rne*), removing the C-terminal scaffold for degradosome assembly, often prevents sRNA-mediated degradation of mRNA targets (15, 31, 32). If translational regulation is the primary function of an sRNA on a given mRNA target, the regulation should be preserved in *rne* mutant backgrounds. For SgrS targets, the regulatory hierarchy is mostly preserved in an *rne701* degradosome mutant background (Fig. 7, compare C and E), suggesting that for most targets, regulation of RNA stability is not the primary mechanism of control by SgrS. Interestingly, the high-priority target *ptsG* was a notable exception. In the wild-type background, *ptsG* is the most efficiently-regulated target (Fig. 7C), whereas in the *rne701* host, it is weakly regulated. This defect could be overcome by increasing SgrS expression levels (Fig. S6B). This result suggests that RNase E-dependent degradation of *ptsG* mRNA is more important for its efficient regulation by SgrS compared to other targets, where efficient regulation does not depend on subsequent target degradation. This is consistent with the fact that *ptsG* mRNA levels decrease at least 10-fold whereas other targets exhibit a modest 2-fold decrease in mRNA levels upon SgrS expression (17). Our recent study quantifying SgrS-dependent mRNA degradation at single molecule resolution indicated that *ptsG* mRNA exhibits faster degradation kinetics than *manXYZ* mRNA (31), which could

370 enhance the efficiency of regulation in a wild-type but not *rne701* mutant background
371 where translational regulation and mRNA degradation are uncoupled.

372 One of our ultimate goals is to define at a molecular level the mechanisms by
373 which sRNAs select and prioritize regulation of their targets. The current study
374 implicates features of sRNA-mRNA interactions such as number and strength of sRNA
375 binding sites on each mRNA target and accessory factors such as RNase E in dictating
376 regulatory hierarchy. Another factor that is likely to play an important role in setting
377 regulatory priority is the RNA chaperone Hfq. EMSAs demonstrated Hfq binding to
378 *ptsG*, *manX*, *purR*, *yigL*, *asdI*, *asdII* and *asdI-II* mRNAs (Fig. S7A) with similar K_D values
379 for all targets (Fig. S7B). Previous work has shown that sRNAs compete for binding to
380 Hfq, and this competition affects their regulatory ability (33, 34). Different sRNAs can
381 bind to distinct sites on Hfq and this impacts their regulation of particular targets (34,
382 35). Additional work will be required to determine what role Hfq plays in establishing the
383 hierarchy of regulatory effects in sRNA regulons.

384 Most sRNA-mRNA interactions are conceived of as single binding site
385 interactions, but we have already identified two SgrS targets that deviate from this
386 model and have shown that additional binding sites can play important roles in
387 regulation and change regulation efficiency (17, 25). We have not yet discovered the
388 specific mechanism of regulation of *asd* mRNA by SgrS, but have shown definitively
389 that both binding sites are required for strong regulation. SgrS-dependent control of
390 both transcriptional and translational *asd* reporter fusions is not impacted in RNase E
391 degradosome deficient strains (Fig. 7B,D, Fig. 8B), suggesting that the regulation is not
392 strictly dependent on translation or mRNA turnover. Future work will test the hypothesis

393 that SgrS acts on *asd* mRNA at the level of transcription elongation, perhaps by an
394 attenuation mechanism.

395 In *Vibrio*, quorum sensing-regulated Qrr sRNAs regulate multiple targets by
396 distinct mechanisms and differences in those mechanisms influence the dynamics and
397 strength of regulation (23). Strong and rapid regulation is achieved by sRNAs acting
398 catalytically where the sRNA pairs with and promotes mRNA degradation but is then
399 recycled for use on another mRNA target. A sequestration mechanism, where formation
400 of the sRNA-mRNA complex is the terminal outcome of regulation, results in slower and
401 weaker sRNA-dependent regulation of the target mRNA. For Qrr sRNAs, these
402 regulatory mechanisms seem to depend on which region of the sRNA is pairing with a
403 given target and whether the sRNA-mRNA interaction is strong or weak (23). While
404 some of the same features of SgrS-mRNA interactions may be relevant in determining
405 regulatory efficiency, we note that the SgrS seed sequence responsible for pairing with
406 all mRNA targets characterized thus far is encompassed by a short (~20 nt) mostly
407 single-stranded region of SgrS (12, 15-17). Moreover, we did not see a good correlation
408 between strong versus weak binding in vitro and in vivo regulatory efficiency. It may be
409 true that the “rules” governing regulatory efficiency and specific outcomes are different
410 for each individual sRNA. Work on more model sRNAs will be needed to illuminate
411 broad general principles.

412 Beyond defining interesting molecular features of sRNA-mRNA interactions,
413 defining regulatory hierarchy for sRNA regulons is important for understanding bacterial
414 physiology. The vast majority of sRNA regulons remain undefined, and thus sRNA
415 functions unknown. For novel sRNAs, distinguishing high-priority from weaker targets

may provide crucial clues to the predominant role of the sRNA in cell physiology. For SgrS, the regulatory hierarchy we have defined here is perfectly consistent with growth studies demonstrating the primary importance of SgrS regulation of sugar transport and efflux under glucose-phosphate stress conditions (36). The hierarchy of regulation by sRNAs likely evolved to promote rapid and efficient responses to environmental signals that would provide cells with a competitive growth advantage in their specific niche. It will be critical to develop tools to more rapidly characterize sRNA regulatory hierarchy to better understand functions of the hundreds of uncharacterized sRNAs in diverse bacteria.

MATERIALS AND METHODS

Strain and plasmid construction. List of strains and plasmids used in this study are listed in Table S1. All strains used in this study are derivatives of *E. coli* K-12 strain MG1655. Oligonucleotide primers and 5' biotinylated probes used in this study are listed in Table S2 and were acquired from Integrated DNA Technologies. Chromosomal alleles were moved between strains by P1 *vir* transduction (37) and inserted using λ Red recombination (38, 39).

Translational reporter fusion alleles P_{BAD}-*asdI-II-lacZ* (MBP151F/MBP193R primers), P_{BAD}-*asdI-lacZ* (MBP151F/MBP151R primers) and P_{BAD}-*asdII-lacZ* (MBP193F/MBP193R primers) were constructed by PCR amplifying desired fragments using primers containing homologies to P_{BAD} and *lacZ.* Similarly, transcriptional fusions P_{BAD}-*asdI-II-lacZ* (MBP151F/MBP206R3 primers) and P_{BAD}-*asdI-lacZ* (MBP151F/MBP206R1 primers) were generated by PCR amplification using forward primer with homology to P_{BAD} and reverse primers containing *lacZ* RBS and *lacZ*

homology. PCR products were then recombined into PM1205 strain using λ Red homologous recombination.

Plasmid harboring SgrS under the control of P_{tet0-1} promoter was constructed by PCR amplifying *sgrS* from *E. coli* MG1655 chromosomal DNA using oligos containing NdeI and BamHI restriction sites. Resulting PCR product and vector pZA31R (24) were digested by NdeI and BamHI (New England Biolabs) restriction endonucleases. Digestion products were ligated using DNA Ligase (New England Biolabs) to produce pZAMB1 plasmid containing P_{tet0-1}-*sgrS* allele.

Plasmid pZEMB8 containing P_{lac0-1}-*ptsG-gfp* was constructed by PCR amplifying *ptsG* from MG1655 chromosomal DNA using oligos containing KpnI and EcoRI restriction sites. Resulting PCR products and vector pZE12S (24) were digested by KpnI and EcoRI restriction endonucleases. Digestion products were ligated using DNA Ligase to produce pZEMB2. Superfolder *gfp* (from now on just *gfp*) was amplified from pXG10-SF (40) using oligos containing KpnI and XbaI restriction sites. pZEMB2 and the resulting PCR product were digested with KpnI and XbaI, and ligated with DNA Ligase to produce pZEMB8. Plasmids with translational reporter fusions P_{lac0-1}-*manX-gfp* (pZEMB10), P_{lac0-1}-*yigL-gfp* (pZEMB15), P_{lac0-1}-*purR-gfp* (pZEMB25), P_{lac0-1}-*asdI-gfp* (pZEMB26) and P_{lac0-1}-*asdI-II-gfp* (pZEMB27) were constructed by restriction cloning into pZEMB8 using KpnI and EcoRI restriction endonucleases.

Media and reagents. Bacteria were cultured in Luria-Bertani (LB) broth medium or LB agar plates (37) at 37°C, unless stated otherwise. Bacteria were grown in MOPS (morpholine-propanesulfonic acid) rich defined medium (Teknova) with 0.2% fructose for reporter fluorescence assays. Where necessary, media was supplemented with

462 antibiotics at following concentrations: 100 μg/ml ampicillin (Amp), 25 μg/ml
463 chloramphenicol (Cm), 25 μg/ml kanamycin (Kan) and 50 μg/ml spectinomycin (Spec).
464 Isopropyl β-D-1-thiogalactopyranoside (IPTG) was used at concentrations of 0.1-1.5
465 mM for induction of P_{lac0-1} promoter, anhydrotetracycline (aTc) 0-50 ng/ml for induction
466 of P_{tet0-1} promoter and 0.000002%-0.2% L-arabinose for induction of P_{BAD} promoter,
467 unless otherwise noted. To induce glucose-phosphate stress, 0.5% α-methylglucoside
468 (αMG) was added to the growth medium.
469 **Reporter fluorescence assay.** Bacterial strains were cultured overnight in MOPS rich
470 medium supplemented with 0.2% fructose, Amp, Cm and subcultured 1:100 to fresh
471 medium with appropriate inducers (IPTG, aTc) in 48 well plates. Relative fluorescence
472 units (RFU) and optical density (OD_{600}) were measured over time. “GFP expression”
473 was calculated by plotting RFU over OD_{600} and determining the slopes of linear
474 regression plots for each IPTG concentration in exponentially growing cells in the
475 presence of aTc to induce SgrS expression. “Promoter activity” was calculated by
476 plotting RFU over OD_{600} and determining the slopes of linear regression plots for each
477 IPTG concentration in exponentially growing cells in the absence of aTc.
478 ***In vitro* transcription and radiolabeling**. Template DNA for *in vitro* transcription was
479 generated by PCR using gene-specific oligonucleotides containing the T7 promoter
480 sequence. Following oligonucleotides were used to generate specific template DNA:
481 MBP84F/MBP213R–*ptsG* (+1 to +240), O-JH218/MBP214R–*manX* (+1 to +240),
482 MBP56F/MBP215R–*asdI-II* (+1 to +240), MBP56F/MBP222R–*asdI* (+1 to +110),
483 MBP226F/MBP226R–*asdII* (+71 to +310), MBP65F/MBP174R–*purR* (+1 to +230),
484 MBP216F/MBP216R–*yigL* (-191 to +50 relative to ATG translation start of *yigL*)

485 MBP234F/MBP234R–*gfp* (+1 to +240) and O-JH219/O-JH119 were used to generate
486 full-length *sgrS* template DNA. *In vitro* transcription of DNA templates was performed
487 according to specifications of MEGAscript T7 Kit (Ambion). *In vitro* transcribed RNA was
488 5'-end labeled with radioisotope ^{32}P using the KinaseMax Kit (Ambion). Samples were
489 cleaned by passing through Illustra ProbeQuant G-50 Micro Columns (GE Healthcare).
490 Than samples were cleaned once more with phenol-chloroform: isoamyl alcohol
491 (Ambion) and labeled RNA precipitated with Ethanol:3M NaAc (30:1).
492 **RNA-RNA gel electrophoretic mobility shift assay***.* Different concentrations of
493 unlabeled mRNA were mixed with 0.02 pmol of 5'-end labeled SgrS. Samples were
494 denatured at 95°C for 1 min, placed on ice for 5 min, and incubated at 37°C for 30 min
495 in 1x binding buffer (20mM Tris-HCL (pH 8.0), 1mM DTT, 1mM $MgCl_2$, 20 mM KCl,
496 10mM Na_2HPO_4 (pH 8.0)) (41). Non-denaturing loading buffer was added and samples
497 resolved for 6 h at 40 V on native 5.6% PAGE.
498 **Protein-RNA gel electrophoretic mobility shift assay.** 0.02 pmol of 5'-end labeled
499 mRNA was denatured at 95°C for 1 min., placed on ice for 5 min. Different
500 concentrations of purified Hfq protein (His-tagged) were added. Samples were
501 incubated at 37°C for 30 min in 1x binding buffer (20mM Tris-HCL (pH 8.0), 1mM DTT,
502 1mM $MgCl_2$, 20 mM KCl, 10mM Na_2HPO_4 (pH 8.0)). Non-denaturing loading buffer was
503 added and samples resolved for 1h 30 min at 20 mA on native 4.0% PAGE (41).
504 **SHAPE.** The *asdI-II* RNA (0.15 µM) and SgrS RNA (0.075 µM, 0.15 µM, 0.30 µM, 0.75
505 µM, 1.5 µM, or 3.0 µM) were folded separately as in (42) using a modified SHAPE
506 buffer (100 mM HEPES [pH 8.0], 2 mM $MgCl_2$, 40 mM NaCl). For each SgrS
507 concentration, the SgrS RNA or the equivalent volume of 0.5X TE was added to the

508 *asdI-II* RNA and the samples were incubated at 37°C for 30 min. The RNAs were
509 modified with *N*-methylisatoic anhydride (NMIA, 6.5 mM; Sigma-Aldrich) and collected
510 by ethanol precipitation as in (42). Parallel primer extension inhibition and sequencing
511 reactions were performed using fluorescently labeled primers complementary to the 3'
512 end of the *asdI-II* RNA (5′-AGATCAAAGGCATCCTGAAG, 22.5 nM; Applied
513 Biosystems, ThermoFisher Scientific) as in (43) with minor modifications. Prior to primer
514 binding the RNAs were denatured and snap cooled and the reactions were carried out
515 for 20 min at 52˚C, followed by 5 min at 65˚C. The cDNAs were analyzed on a 3730
516 DNA Analyzer (Applied Biosystems, Inc.). The data were processed and SHAPE
517 reactivity (difference between the frequency of primer extension products at each
518 nucleotide in +NMIA vs. -NMIA samples) was derived using the QuShape software (44).
519 Data for each nucleotide were averaged with statistical outliers removed and normalized
520 using the 2-8% rule (45). Relative reactivity was calculated by subtracting normalized
521 SHAPE reactivity in the absence of the SgrS RNA from reactivity in the presence of the
522 WT or MT SgrS RNA.
523 **Single-molecule fluorescence *in situ* hybridization (smFISH).** The *asdI-lacZ*
524 (MB170), *asdII-lacZ* (MB183) and *asdI-II-lacZ* (MB171) strains were grown overnight at
525 37 ºC, 250 rpm in LB Broth Miller (EMD) with 25 µg/ml kanamycin (Kan) and 50 µg/ml
526 spectinomycin (Spec). The next day, the overnight culture was diluted 100-fold into
527 MOPS EZ rich defined medium (Teknova) with 0.2% (w/w) sodium succinate, 0.02%
528 glycerol and 0.01% L-arabinose, for *asdI-lacZ* and *asdII-lacZ* strains, and was allowed
529 to grow at 37 ºC till the OD_{600} reached 0.15-0.25. The concentration of L-arabinose used
530 for *asdI-II-lacZ* was 0.002%. α-methyl D-glucopyranoside (αMG) (Sigma-Aldrich) was

added to the culture to a desired concentration to introduce sugar phosphate stress and induce SgrS sRNA expression. After 10 minutes of induction, the culture was taken out and fixation was performed by mixing with formaldehyde (Fisher Scientific) at a final concentration of 4%.

Δ*sgrS* and Δ*lacZ* strains were grown in LB Broth Miller (EMD) at 37 ºC, 250 rpm overnight. Then the cultures were diluted 100-fold into MOPS EZ rich defined medium (Teknova) with 0.2% glucose and allowed to grow at 37 ºC till the OD_{600} reached 0.2. The cells were then fixed by mixing with formaldehyde (Fisher Scientific) at a final concentration of 4%. TK310 cells were grown overnight, similar to the knockout strains. The overnight culture was then diluted 100-fold into MOPS EZ rich defined medium (Teknova) with 0.2% glucose and 1 mM isopropyl β-D-1-thiogalactopyranoside (IPTG, Sigma-Aldrich) and allowed to grow at 37 ºC for 30 minutes. The cells were then fixed in the same procedure as mentioned before.

The fixation and permeabilization of the cells were done using the methods published previously (46). After fixing with 4% formaldehyde, the cells were incubated at room temperature for 30 minutes. The cells were then centrifuged at 600 g for 7 minutes and the pellets were washed with 1X PBS 3 times. The cells were then permeabilized with 70% ethanol for 1 hour at room temperature and stored at 4 ºC before fluorescence *in situ* hybridization.

The smFISH probes were designed using Stellaris Probe Designer and the orders were placed from Biosearch Technologies (https://www.biosearchtech.com/). The labeling of the probes was performed using equal volumes of each probe. The final volume of sodium bicarbonate was adjusted to 0.1 M by adding 1/9 reaction volume of 1

554 M sodium bicarbonate (pH = 8.5). The probe solution was mixed with 0.05-0.25 mg of
555 Alexa Fluor 647 or Alexa Fluor 568 succinimidyl ester (Life Technologies) dissolved in 5
556 µL DMSO. The dye was kept about 20-25 fold in molar excess relative to the probes.
557 After incubation with gentle vortexing in the dark at 37 ºC overnight, the reaction was
558 quenched by adding 1/9 reaction volume of 3 M sodium acetate (pH = 5). Unconjugated
559 dyes were removed by ethanol precipitation first and then by P-6 Micro Bio-Spin
560 Column (Bio-Rad).

561 A previously published protocol (46) was used for the hybridization procedure. 60
562 µl of permeabilized cells were washed with FISH wash solution (10% formamide in 2X
563 SSC (Saline Sodium Citrate) buffer) and resuspended in 15 µl hybridization buffer (10%
564 dextran sulfate, 1 mg/ml *E. Coli* tRNA, 0.2 mg/ml BSA, 2 mM vanadyl ribonucleoside
565 complexes, 10% formamide in 2X SSC) with probes. The number of probes used for
566 sRNA SgrS was 9 and they were labeled with Alexa Fluor 647. The number of probes
567 for mRNA *lacZ* was 24 and they were labeled with Alexa Fluor 568. The concentration
568 of the labeled probes for SgrS and *lacZ* mRNA were 50 nM and 15 nM each. The
569 reactions were incubated in the dark at 30 ºC overnight. The cells were then
570 resuspended in 20X volume FISH wash solution and centrifuged. They were then
571 resuspended in FISH wash solution, incubated for 30 minutes at 30 ºC and centrifuged
572 and this was repeated 3 times. The cells were pelleted after the final washing step and
573 resuspended in 20 µl 4X SSC and stored at 4 ºC for imaging. The labeled cells were
574 immobilized in poly-L-lysine (Sigma-Aldrich) treated 1.0 borosilicate chambered
575 coverglass (Thermo Scientific^{TM} Nunc^{TM} Lab-Tek^{TM}). They were then imaged with
576 imaging buffer (50 mM Tris-HCl (pH = 8.0), 10% glucose, 1% β-mercaptoethanol

(Sigma-Aldrich), 0.5 mg/ml glucose oxidase (Sigma-Aldrich) and 0.2% catalase (Calbiochem) in 2X SSC).

Single-molecule localization-based super-resolution imaging. An Olympus IX-71 inverted microscope with a 100X NA 1.4 SaPo oil immersion objective was used for the 3D super-resolution imaging. The lasers used for two-color imaging were Sapphire 568-100 CW CDRH, Coherent (568nm) and DL640-100-AL-O, Crystalaser (647nm) and DL405-025, Crystalaser (405nm) was used for the reactivation of Alexa 647 and Alexa 568 fluorophores. The laser excitation was controlled using mechanical shutters (LS6T2, Uniblitz). A dichroic mirror (Di01-R405/488/561/635, Semrock) was used to reflect the laser lines to the objective. The objective collected the emission signals and then they made their way through an emission filter (FF01-594/730-25, Semrock for Alexa 647 or HQ585/70M 63061, Chroma for Alexa 568) and excitation laser was cleaned up using notch filters (ZET647NF, Chroma, NF01-568/647-25x5.0 and NF01-568U-25, Semrock). They were then imaged on a 512x512 Andor EMCCD camera (DV887ECS-BV, Andor Tech). Astigmatism was introduced by placing a cylindrical lens with a focal length of 2 m (SCX-50.8-1000.0-UV-SLMF-520-820, CVI Melles Griot) in the emission path between two relay lenses with focal lengths of 100 mm and 150 mm each and this helped us to do 3D imaging. In this setup, each pixel corresponded to 100 nm. We used the CRISP (Continuous Reflective Interface Sample Placement) system (ASI) to keep the z-drift of the setup to a minimum. The image acquisition was controlled using the storm-control software written in Python by Zhuang's group and available at GitHub.

The imaging of the sample began with a DIC image of the sample area. Subsequently two-color super-resolution imaging was performed. 647nm excitation was used first and after image acquisition was completed for Alexa Fluor 647, 568nm excitation was used to image Alexa Fluor 568. 405nm laser power was increased slowly to compensate for fluorophore bleaching and also to maintain moderate signal density. We stopped imaging when most of the fluorophores had photobleached and the highest reactivation laser power was reached.

The raw data acquired using the acquisition software was analyzed using the same method as described in previously published work (31), which was a modification of the algorithm published by Zhuang's group (47, 48). The clustering analysis on the localization data was performed using MATLAB codes in the same method as described previously (31). Background signal was estimated using Δ*sgrS* and Δ*lacZ* strains and they were prepared, imaged and analyzed as described before. TK310 cells were prepared, imaged and analyzed in the same way as a low copy *lacZ* mRNA sample for copy number calculation. The copy number calculation was also performed using MATLAB codes as described previously (31).

ACKNOWLEDGEMENTS

We would like to extend a special thank you to Erel Levine for providing plasmids. We are grateful to Jennifer Rice, Rich Yemm, Divya Balasubramanian, Chelsea Lloyd, Alisa King, Jessica Kelliher and other current and past members of the Vanderpool lab for strains, plasmids and valuable advice. We appreciate and thank Prof. James Slauch and members of his lab for fruitful discussions.

FUNDING

National Institutes of Health R01 GM092830 (M.B. and C.K.V.), R01 GM112659 (M.B., M.S.A., T.H., J.Z., and A.P.), R35 GM122569 (T.H., J.Z., and A.P.), R01 GM047823 (T.H.), T32 GM086252 (J.F.); National Science Foundation PHY 1430124 (T.H., J.Z., and A.P); University of Illinois Department of Microbiology James R. Beck Fellowship (M. B.).

REFERENCES

1. Gisela Storz RH. 2011. Bacterial Stress Responses, Second Edition doi:10.1128/9781555816841. ASM Press, Washington DC.
2. Fang FC, Frawley ER, Tapscott T, Vazquez-Torres A. 2016. Bacterial Stress Responses during Host Infection. Cell Host Microbe 20:133-43.
3. Georg J, Hess W. 2011. cis-antisense RNA, another level of gene regulation in bacteria. Microbiology and molecular biology reviews : MMBR 75:286-300.
4. Storz G, Vogel J, Wassarman KM. 2011. Regulation by small RNAs in bacteria: expanding frontiers. Mol Cell 43:880-91.
5. Carroll RK, Weiss A, Broach WH, Wiemels RE, Mogen AB, Rice KC, Shaw LN. 2016. Genome-wide Annotation, Identification, and Global Transcriptomic Analysis of Regulatory or Small RNA Gene Expression in Staphylococcus aureus. MBio 7:e01990-15.
6. Koo JT, Lathem WW. 2012. Global discovery of small noncoding RNAs in pathogenic Yersinia species. Adv Exp Med Biol 954:305-14.
7. Zhang A, Wassarman KM, Rosenow C, Tjaden BC, Storz G, Gottesman S. 2003. Global analysis of small RNA and mRNA targets of Hfq. Mol Microbiol 50:1111-24.
8. Salvail H, Masse E. 2012. Regulating iron storage and metabolism with RNA: an overview of posttranscriptional controls of intracellular iron homeostasis. Wiley Interdiscip Rev RNA 3:26-36.
9. Sharma CM, Papenfort K, Pernitzsch SR, Mollenkopf HJ, Hinton JC, Vogel J. 2011. Pervasive post-transcriptional control of genes involved in amino acid metabolism by the Hfq-dependent GcvB small RNA. Mol Microbiol 81:1144-65.
10. Bobrovskyy M, Vanderpool CK. 2013. Regulation of bacterial metabolism by small RNAs using diverse mechanisms. Annu Rev Genet 47:209-32.
11. Bobrovskyy M, Vanderpool CK, Richards GR. 2015. Small RNAs Regulate Primary and Secondary Metabolism in Gram-negative Bacteria. Microbiol Spectr 3.
12. Vanderpool CK, Gottesman S. 2004. Involvement of a novel transcriptional activator and small RNA in post-transcriptional regulation of the glucose phosphoenolpyruvate phosphotransferase system. Mol Microbiol 54:1076-89.
13. Vanderpool CK, Gottesman S. 2007. The novel transcription factor SgrR coordinates the response to glucose-phosphate stress. J Bacteriol 189:2238-48.
14. Rice JB, Balasubramanian D, Vanderpool CK. 2012. Small RNA binding-site multiplicity involved in translational regulation of a polycistronic mRNA. Proceedings of the National Academy of Sciences of the United States of America 109:E2691-8.
15. Rice JB, Vanderpool CK. 2011. The small RNA SgrS controls sugar-phosphate accumulation by regulating multiple PTS genes. Nucleic Acids Res 39:3806-19.
16. Papenfort K, Sun Y, Miyakoshi M, Vanderpool CK, Vogel J. 2013. Small RNA-mediated activation of sugar phosphatase mRNA regulates glucose homeostasis. Cell 153:426-37.
17. Bobrovskyy M, Vanderpool CK. 2016. Diverse mechanisms of post-transcriptional repression by the small RNA regulator of glucose-phosphate stress. Mol Microbiol 99:254-73.
18. Chevance FF, Hughes KT. 2008. Coordinating assembly of a bacterial macromolecular machine. Nat Rev Microbiol 6:455-65.
19. Syed KA, Beyhan S, Correa N, Queen J, Liu J, Peng F, Satchell KJ, Yildiz F, Klose KE. 2009. The Vibrio cholerae flagellar regulatory hierarchy controls expression of virulence factors. J Bacteriol 191:6555-70.
20. Tonner PD, Pittman AM, Gulli JG, Sharma K, Schmid AK. 2015. A regulatory hierarchy controls the dynamic transcriptional response to extreme oxidative stress in archaea. PLoS Genet 11:e1004912.

678 21. Yu H, Gerstein M. 2006. Genomic analysis of the hierarchical structure of regulatory
679 networks. Proc Natl Acad Sci U S A 103:14724-31.
680 22. Gao R, Stock AM. 2015. Temporal hierarchy of gene expression mediated by
681 transcription factor binding affinity and activation dynamics. MBio 6:e00686-15.
682 23. Feng L, Rutherford ST, Papenfort K, Bagert JD, van Kessel JC, Tirrell DA, Wingreen NS,
683 Bassler BL. 2015. A qrr noncoding RNA deploys four different regulatory mechanisms to
684 optimize quorum-sensing dynamics. Cell 160:228-40.
685 24. Levine E, Zhang Z, Kuhlman T, Hwa T. 2007. Quantitative characteristics of gene
686 regulation by small RNA. PLoS Biol 5:e229.
687 25. Rice JB, Balasubramanian D, Vanderpool CK. 2012. Small RNA binding-site multiplicity
688 involved in translational regulation of a polycistronic mRNA. Proc Natl Acad Sci U S A
689 109:E2691-8.
690 26. Busch A, Richter AS, Backofen R. 2008. IntaRNA: efficient prediction of bacterial sRNA
691 targets incorporating target site accessibility and seed regions. Bioinformatics 24:2849-
692 56.
693 27. Wright PR, Georg J, Mann M, Sorescu DA, Richter AS, Lott S, Kleinkauf R, Hess WR,
694 Backofen R. 2014. CopraRNA and IntaRNA: predicting small RNA targets, networks and
695 interaction domains. Nucleic Acids Res 42:W119-23.
696 28. Morita T, Kawamoto H, Mizota T, Inada T, Aiba H. 2004. Enolase in the RNA
697 degradosome plays a crucial role in the rapid decay of glucose transporter mRNA in the
698 response to phosphosugar stress in Escherichia coli. Mol Microbiol 54:1063-75.
699 29. Morita T, Maki K, Aiba H. 2005. RNase E-based ribonucleoprotein complexes:
700 mechanical basis of mRNA destabilization mediated by bacterial noncoding RNAs.
701 Genes Dev 19:2176-86.
702 30. Kawamoto H, Koide Y, Morita T, Aiba H. 2006. Base-pairing requirement for RNA
703 silencing by a bacterial small RNA and acceleration of duplex formation by Hfq. Mol
704 Microbiol 61:1013-22.
705 31. Fei J, Singh D, Zhang Q, Park S, Balasubramanian D, Golding I, Vanderpool CK, Ha T.
706 2015. RNA biochemistry. Determination of in vivo target search kinetics of regulatory
707 noncoding RNA. Science 347:1371-4.
708 32. Morita T, Mochizuki Y, Aiba H. 2006. Translational repression is sufficient for gene
709 silencing by bacterial small noncoding RNAs in the absence of mRNA destruction. Proc
710 Natl Acad Sci U S A 103:4858-63.
711 33. Moon K, Gottesman S. 2011. Competition among Hfq-binding small RNAs in Escherichia
712 coli. Mol Microbiol 82:1545-62.
713 34. Santiago-Frangos A, Kavita K, Schu DJ, Gottesman S, Woodson SA. 2016. C-terminal
714 domain of the RNA chaperone Hfq drives sRNA competition and release of target RNA.
715 Proc Natl Acad Sci U S A 113:E6089-E6096.
716 35. Schu DJ, Zhang A, Gottesman S, Storz G. 2015. Alternative Hfq-sRNA interaction
717 modes dictate alternative mRNA recognition. EMBO J 34:2557-73.
718 36. Sun Y, Vanderpool CK. 2011. Regulation and function of Escherichia coli sugar efflux
719 transporter A (SetA) during glucose-phosphate stress. J Bacteriol 193:143-53.
720 37. Miller JH. 1972. Experiments in Bacterial Genetics. Cold Spring Harbor Laboratory
721 Press, Cold Spring Harbor, NY.
722 38. Datsenko KA, Wanner BL. 2000. One-step inactivation of chromosomal genes in
723 Escherichia coli K-12 using PCR products. Proc Natl Acad Sci U S A 97:6640-5.
724 39. Yu D, Ellis HM, Lee EC, Jenkins NA, Copeland NG, Court DL. 2000. An efficient
725 recombination system for chromosome engineering in Escherichia coli. Proc Natl Acad
726 Sci U S A 97:5978-83.

40. Corcoran CP, Podkaminski D, Papenfort K, Urban JH, Hinton JC, Vogel J. 2012. Superfolder GFP reporters validate diverse new mRNA targets of the classic porin regulator, MicF RNA. Mol Microbiol 84:428-45.
41. Morita T, Maki K, Aiba H. 2012. Detection of sRNA-mRNA interactions by electrophoretic mobility shift assay. Methods Mol Biol 905:235-44.
42. Wilkinson KA, Merino EJ, Weeks KM. 2006. Selective 2'-hydroxyl acylation analyzed by primer extension (SHAPE): quantitative RNA structure analysis at single nucleotide resolution. Nat Protoc 1:1610-6.
43. Mortimer SA, Weeks KM. 2009. Time-resolved RNA SHAPE chemistry: quantitative RNA structure analysis in one-second snapshots and at single-nucleotide resolution. Nat Protoc 4:1413-21.
44. Karabiber F, McGinnis JL, Favorov OV, Weeks KM. 2013. QuShape: rapid, accurate, and best-practices quantification of nucleic acid probing information, resolved by capillary electrophoresis. RNA 19:63-73.
45. McGinnis JL, Duncan CD, Weeks KM. 2009. High-throughput SHAPE and hydroxyl radical analysis of RNA structure and ribonucleoprotein assembly. Methods Enzymol 468:67-89.
46. So LH, Ghosh A, Zong C, Sepulveda LA, Segev R, Golding I. 2011. General properties of transcriptional time series in Escherichia coli. Nat Genet 43:554-60.
47. Huang B, Wang W, Bates M, Zhuang X. 2008. Three-dimensional super-resolution imaging by stochastic optical reconstruction microscopy. Science 319:810-3.
48. Rust MJ, Bates M, Zhuang X. 2006. Sub-diffraction-limit imaging by stochastic optical reconstruction microscopy (STORM). Nat Methods 3:793-5.
49. Lorenz R, Luntzer D, Hofacker IL, Stadler PF, Wolfinger MT. 2016. SHAPE directed RNA folding. Bioinformatics 32:145-7.
50. Ishikawa H, Otaka H, Maki K, Morita T, Aiba H. 2012. The functional Hfq-binding module of bacterial sRNAs consists of a double or single hairpin preceded by a U-rich sequence and followed by a 3' poly(U) tail. RNA 18:1062-74.

FIGURE LEGENDS

Figure 1. Model for SgrS target prioritization during glucose-phosphate stress.

Glucose or the analogs αMG and 2-deoxyglucose are phosphorylated during transport through the phosphotransferase system proteins $EIICB^{Glc}$ (PtsG) or $EIICD^{Man}$ (ManYZ). If sugar-phosphates are not metabolized, the glucose-phosphate stress response is triggered, and the transcription factor SgrR becomes active and promotes *sgrS* transcription. The RNA chaperone Hfq promotes SgrS-mediated translational repression of *ptsG* and *manXYZ* mRNAs, reducing synthesis of sugar transporters. SgrS stabilizes *yigL* mRNA, promoting sugar phosphatase (YigL) synthesis. SgrS-mediated repression of *asd, purR, folE* and *adiY* likely reroutes metabolism to restore homeostasis during

766 stress recovery. The hypothetical sequence of regulatory events following stress
767 induction is represented from left to right as SgrS levels increase over time. When SgrS
768 concentrations are low, only the highest priority targets are regulated. When stress
769 persists and concentrations of SgrS increase, lower priority targets are regulated.
770 **Figure 2. Efficiency of target regulation by SgrS.** A) Representation of genetic
771 constructs in two compatible plasmids used to study target regulation by SgrS. One
772 plasmid contains full-length SgrS under the control of the aTc-inducible P_{tet} promoter. A
773 second plasmid contains a P_{lac} promoter and the relevant region encoding each SgrS
774 target (including the SgrS binding site) translationally fused to a superfolder *gfp* (*sfgfp*)
775 reporter gene. B-F) Regulated activity was plotted as a function of basal activity (see
776 text for description) for (B) *ptsG*, (C) *manX*, (D) *purR,* (E) *asdI,* and (F) *yigL* fused to
777 *sfgfp* reporter gene. Without SgrS-mediated regulation we obtained a line with a slope
778 =1. The plots with slopes <1, indicate repression of (B) *ptsG*, (C) *manX*, (D) *purR* and
779 (E) *asdI* by SgrS. The plot with a slope of >1 are indicative of activation of (F) *yigL*.
780 **Figure 3. Regulatory hierarchy established by SgrS.** Regulated activity was plotted
781 as a function of basal activity for *ptsG*, *manX*, *purR, asdI,* and *yigL* fusions. Lack of
782 SgrS regulation is indicated by a line with a slope =1. The plots with slopes <1, indicate
783 repression (*ptsG*, *manX*, *purR* and *asdI*) by SgrS. The plot with slope >1 indicates
784 activation (*yigL*). Target fusion activity was monitored at different levels of SgrS
785 induction by aTc: (A) 10 ng/ml, (B) 20 ng/ml, (C) 30 ng/ml, (D) 40 ng/ml, (E) 50 ng/ml.
786 **Figure 4. SgrS binding with target mRNAs *in vitro***. A) SgrS was labeled with ^{32}P and
787 incubated with unlabeled target transcripts at final concentrations of 0µM - 16 µM .
788 Electrophoretic mobility shift assays (EMSAs) were performed after incubating full-

789 length SgrS (+1 to +227) with its target transcripts (A) *ptsG* (+1 to +240), *manX* (+1 to
790 +240), *purR* (+1 to +230), *yigL* (-191 to +50 relative to ATG translation start of *yigL*),
791 *asdI* (+1 to +110), and *asdII* (+71 to +310). B-D) Targets transcripts (B) *ptsG* (+1 to
792 +240), (C) *manX* (+1 to +240), (D) *asdI* (+1 to +110) were labeled with ^{32}P and
793 incubated with unlabeled SgrS. EMSAs were performed to resolve complex formation.
794 Band densities were measured for biological replicates (n, top left) and plotted to
795 determine dissociation constant (K_D, bottom right) values for (B) *ptsG*, (C) *manX*, and
796 (D) *asdI*. E) EMSA of radiolabeled SgrS in the presence of increasing concentrations of
797 *asdI-II* transcript. Shift in mobility corresponding to one or two SgrS bound to *asdI-II* is
798 denoted as Site I-SgrS* and Sites I-II-SgrS* respectively. F) Quantification of SgrS
799 binding with radiolabeled *asdI-II* (+1 to +240), as described above.
800 **Figure 5. Secondary structure of 5' end of *asd*.** A) Diagram showing base-pairing
801 interactions of SgrS with binding sites I and II of *asd* mRNA. B) Energy of interaction
802 predicted by IntaRNA (26). "Structured" indicates pairing between full length SgrS (+1 to
803 +227) and *asdI-II* (+1 to +180). Plotted is the energy of interactions at either site I (*asdI*)
804 or site II (*asdII*). "Isolated" indicates interactions between isolated binding sites: SgrS
805 (+158 to +176) with *asdI* (+31 to +49) and SgrS (+158 to +178) pairing with *asdII* (+110
806 to +129). C) The structure of the *asdI-II* RNA alone or in complex with SgrS was probed
807 with NMIA and the modified RNA was analyzed by primer extension inhibition. SHAPE
808 reactivity (difference between the frequency of primer extension products at each
809 nucleotide in +NMIA vs. -NMIA samples) was then used as a parameter in the Vienna
810 RNAprobing WebServer (49) to predict the secondary structure of the *asdI-II* RNA.
811 Colors indicate SHAPE reactivity as following: red, highly reactive (≥ 0.8); gold, reactive

(0.4-0.79); green, moderately reactive (0.2-0.39); blue, minimally reactive (0.1-0.19); grey, unreactive (< 0.01). Distinct structures were observed in the absence of SgrS and in the presence of saturating concentrations of SgrS. The SHAPE reactivity of *asdI-II* RNA alone (left) or in the presence of 5-fold excess SgrS (right) is mapped to the predicted secondary structures. (D) SHAPE reactivity as a function of SgrS concentration for each binding site (top, site I; bottom, site II). Only nucleotides with a significant (≥ 0.1) change in reactivity are shown. Error bars denote SEM, n = 9. (E) Relative SHAPE reactivity (difference in the SHAPE reactivity in the presence of SgrS vs. the absence of SgrS) of the *asdI-II* RNA in the presence of wild-type (top) or mutant (bottom) SgrS. Error bars denote SEM, n = 9 (WT), 6 (MT). The *asdI-II* RNA nucleotides are numbered below the X-axis and the SgrS binding sites are indicated.

Figure 6. STORM imaging of SgrS regulation of *asd* variants. A) Illustration of *asdI-II*, *asdI* and *asdII* translationally fused to *lacZ* reporter with SgrS binding sites I and II marked. B-D) 2D projection of 3D super-resolution images of SgrS and *lacZ* mRNA for the different *asd-lacZ* variants, labeled by smFISH, before and after 10 min induction with 1% αMG. (B), (C) and (D) correspond to *asdI-lacZ*, *asdII-lacZ,* and *asdI-II-lacZ* shown in (A). Probability distributions of RNA copy numbers in individual cells for 30-250 cells are plotted next to the representative images.

Figure 7. SgrS binding cooperativity allows for improved repression of *asd* translation. A) Illustration of *asdI* and *asdI-II* constructs with SgrS binding sites marked. Graphs show comparison of SgrS regulation of *asdI* and *asdI-II* variants in (B) wild-type and (D) *rne701* mutant by plotting regulated activity over basal activity at various SgrS expression levels (20-100 ng/ml aTc). Regulatory hierarchy of SgrS targets in (C) wild-

835 type and (E) *rne701* mutant strains. Regulation of target genes at one SgrS expression
836 level (40 ng/ml aTc) are compared by plotting regulated activity over basal activity of the
837 *gfp* reporter.

838 **Figure 8. SgrS regulation of transcriptional *asd-lacZ* fusions.** β-galactosidase
839 activity of (A) *asdI-lacZ* (+1 to +64) and *asdI-II-lacZ* (+1 to +277) was (B) assayed in
840 response to SgrS expression from a plasmid (and vector control) in WT and *rne701*
841 background strains.

842

843 **Figure S1. Regulation of *ptsG* fusion by SgrS.** Example plots of *ptsG-gfp*
844 translational fusion activity (RFU) over growth (OD_{600}) at various IPTG inducer
845 concentrations at (A) basal (uninduced) or (B-F) increasing SgrS expression levels.
846 Slopes of the linear regression plots for each IPTG concentration were calculated to
847 obtain (A) “basal expression” and (B-F) “regulated activity” values.

848 **Figure S2. Inducer concentration-dependent activity of target fusions.** (A) Basal
849 activity (0 ng/ml aTc) or (B-F) regulated activity (10-50 ng/ml aTc) of *ptsG*, *manX*, *purR*,
850 *asdI*, *asdI-II* and *yigL* fusions at varying IPTG concentrations (0-1.5 mM IPTG).

851 **Figure S3: SHAPE analysis of *asdI-II* RNA.** (A-G) SHAPE reactivity of the *asdI-II* RNA
852 alone and in complex with increasing concentrations of SgrS (0.5, 1, 2, 5, 10, or 20X).
853 The structure of the *asdI-II* RNA in the absence and presence of SgrS was probed with
854 NMIA and the modified RNA was analyzed by primer extension inhibition. SHAPE
855 reactivity is the difference between the frequency of primer extension products at each
856 nucleotide in +NMIA vs. -NMIA samples. Colors indicate SHAPE reactivity as following:
857 red, highly reactive (≥ 0.8); gold, reactive (0.4-0.79); green, moderately reactive (0.2-

858 0.39); blue, minimally reactive (0.1-0.19); grey, unreactive (< 0.01). (H) Relative SHAPE
859 reactivity of the *asdI-II* RNA in the presence of wild-type vs mutant SgrS. Relative
860 reactivity is the difference in the SHAPE reactivity in the presence of wild-type and
861 mutant SgrS. Error bars denote SEM, n = 9. The *asdI-II* RNA nucleotides are numbered
862 below the X-axis and the SgrS binding sites are indicated. (I-J) SHAPE reactivity as a
863 function of mutant SgrS concentration for each binding site (I, site I; J, site II). The same
864 nucleotides as in Fig. 5D are shown. Error bars denote SEM, n = 6.

865 **Figure S4. Quantification of SgrS and *asd* mRNA variants using STORM.** Copy
866 number of *lacZ* mRNA vs. SgrS in 30-250 individual cells for the different *asd-*
867 *lacZ* variants, (A-B) *asdI-lacZ*, (C-D) *asdII-lacZ*, and (E-F) *asdI-II-lacZ*, before (A,C,E)
868 and after (B,D,F) 10 min 1% αMG induction.

869 **Figure S5. Inducer concentration-dependent activity of target-*gfp* fusions.** (A)
870 Basal activity (0 ng/ml aTc) or (B-F) regulated activity (20-100 ng/ml aTc) of *ptsG*,
871 *manX*, *purR*, *asdI*, *asdI-II* and *yigL* fusions at varying IPTG concentrations (0-1.5 mM
872 IPTG).

873 **Figure S6. Regulatory hierarchy established by SgrS in the RNase E mutant**
874 **strain.** A) Regulated activity was plotted as a function of basal activity (see text for
875 description) for *ptsG*, *manX*, *purR, yigL*, *asdI* and *asdI-II* fused to *sfgfp* reporter gene in
876 the *rne701* mutant strain. Target fusion activity was monitored at different levels of SgrS
877 induction by aTc: 20 ng/ml, 40 ng/ml, 60 ng/ml, 80 ng/ml, 100 ng/ml. B) Target
878 regulation at different SgrS expression levels in the *rne701* mutant strain was compared
879 to determine regulatory hierarchy. Without SgrS-mediated regulation we obtained a line
880 with a slope =1. The plots with slopes <1, indicate repression of *ptsG*, *manX*, *purR, asdI*

881 and *asdI-II* by SgrS. The plot with the slope of >1 is indicative of activation of *yigL*. B)
882 Regulated activity was plotted as a function of basal activity for *ptsG*, *manX*, *purR, asdI,*
883 and *yigL* fusions.
884 **Figure S7. Hfq binding with target mRNAs *in vitro*.** A) Target transcripts *ptsG* (+1 to
885 +240), *manX* (+1 to +240), *purR* (+1 to +230), *yigL* (-191 to +50 relative to ATG
886 translation start of *yigL*) *, asdI* (+1 to +110)*, asdII* (+71 to +310) and *asdI-II* (+1 to +240)
887 were labeled with ^{32}P and incubated with appropriate concentrations of Hfq protein.
888 EMSAs were performed to resolve complex formation. Complexes of increasing size are
889 marked I-IV, as was previously noted for Hfq (50). B) Band densities were measured for
890 biological replicates (n, top left) and plotted to determine dissociation constant (K_D,
891 bottom right) values.
892 **Table S1. Strains and plasmids used in this study.**
893 **Table S2. Oligonucleotides used in this study.**

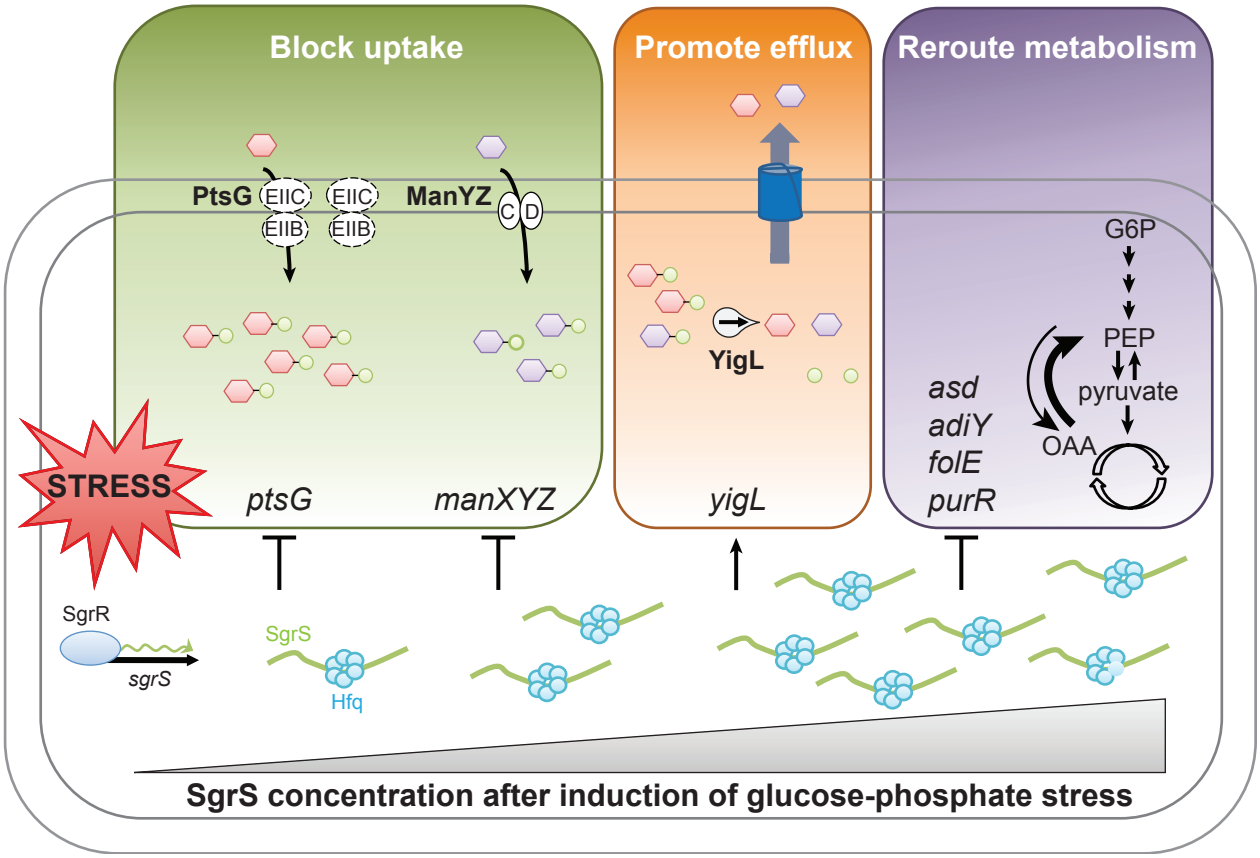

Figure 1. Model for SgrS target prioritization during glucose-phosphate stress. Glucose or the analogs αMG and 2-deoxyglucose are phosphorylated during transport through the phosphotransferase system proteins EIICB^{Glc} (PtsG) or EIICD^{Man} (ManYZ). If sugar-phosphates are not metabolized, the glucose-phosphate stress response is triggered, and the transcription factor SgrR becomes active and promotes *sgrS* transcription. The RNA chaperone Hfq promotes SgrS-mediated translational repression of *ptsG* and *manXYZ* mRNAs, reducing synthesis of sugar transporters. SgrS stabilizes *yigL* mRNA, promoting sugar phosphatase (YigL) synthesis. SgrS-mediated repression of *asd, purR, folE* and *adiY* likely reroutes metabolism to restore homeostasis during stress recovery. The hypothetical sequence of regulatory events following stress induction is represented from left to right as SgrS levels increase over time. When SgrS concentrations are low, only the highest priority targets are regulated. When stress persists and concentrations of SgrS increase, lower priority targets are regulated.

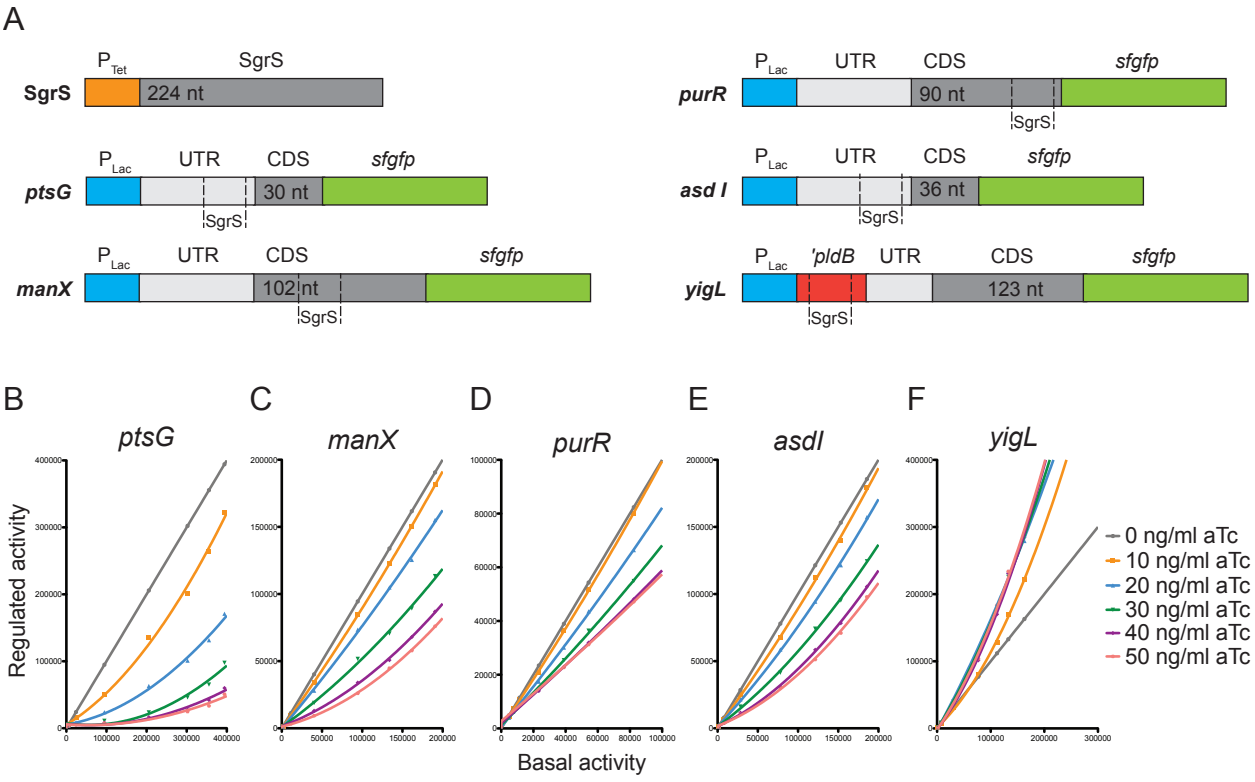

Figure 2. Efficiency of target regulation by SgrS. A) Representation of genetic constructs in two compatible plasmids used to study target regulation by SgrS. One plasmid contains full-length SgrS under the control of the aTc-inducible P_{tet} promoter. A second plasmid contains a P_{lac} promoter and the relevant region encoding each SgrS target (including the SgrS binding site) translationally fused to a superfolder *gfp* (*sfgfp*) reporter gene. B-F) Regulated activity was plotted as a function of basal activity (see text for description) for (B) *ptsG*, (C) *manX*, (D) *purR,* (E) *asdI,* and (F) *yigL* fused to *sfgfp* reporter gene. Without SgrS-mediated regulation we obtained a line with a slope =1. The plots with slopes <1, indicate repression of (B) *ptsG*, (C) *manX*, (D) *purR* and (E) *asdI* by SgrS. The plot with a slope of >1 are indicative of activation of (F) *yigL*.

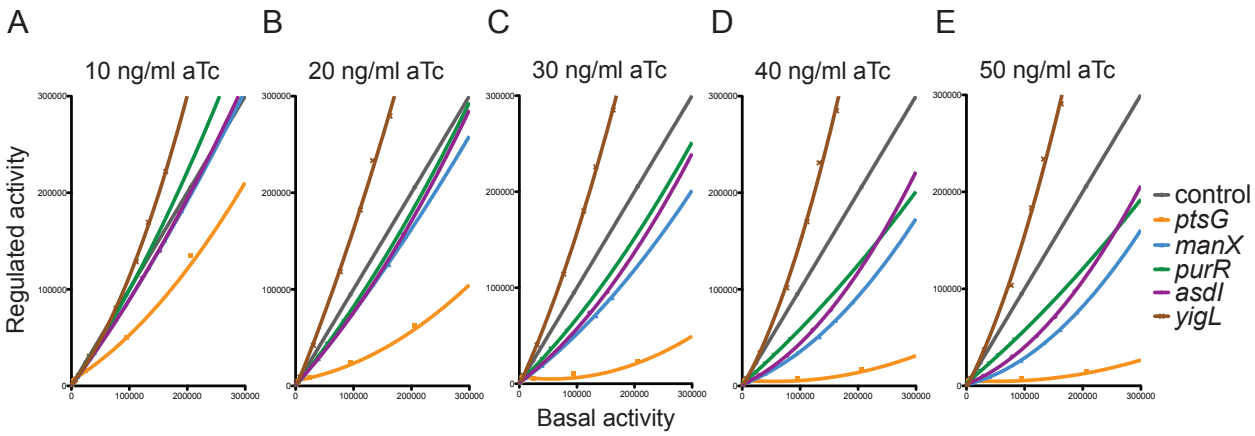

Figure 3. Regulatory hierarchy established by SgrS. Regulated activity was plotted as a function of basal activity for *ptsG*, *manX*, *purR, asdI,* and *yigL* fusions. Lack of SgrS regulation is indicated by a line with a slope =1. The plots with slopes <1, indicate repression (*ptsG*, *manX*, *purR* and *asdI*) by SgrS. The plot with slope >1 indicates activation (*yigL*). Target fusion activity was monitored at different levels of SgrS induction by aTc: (A) 10 ng/ml, (B) 20 ng/ml, (C) 30 ng/ml, (D) 40 ng/ml, (E) 50 ng/ml.

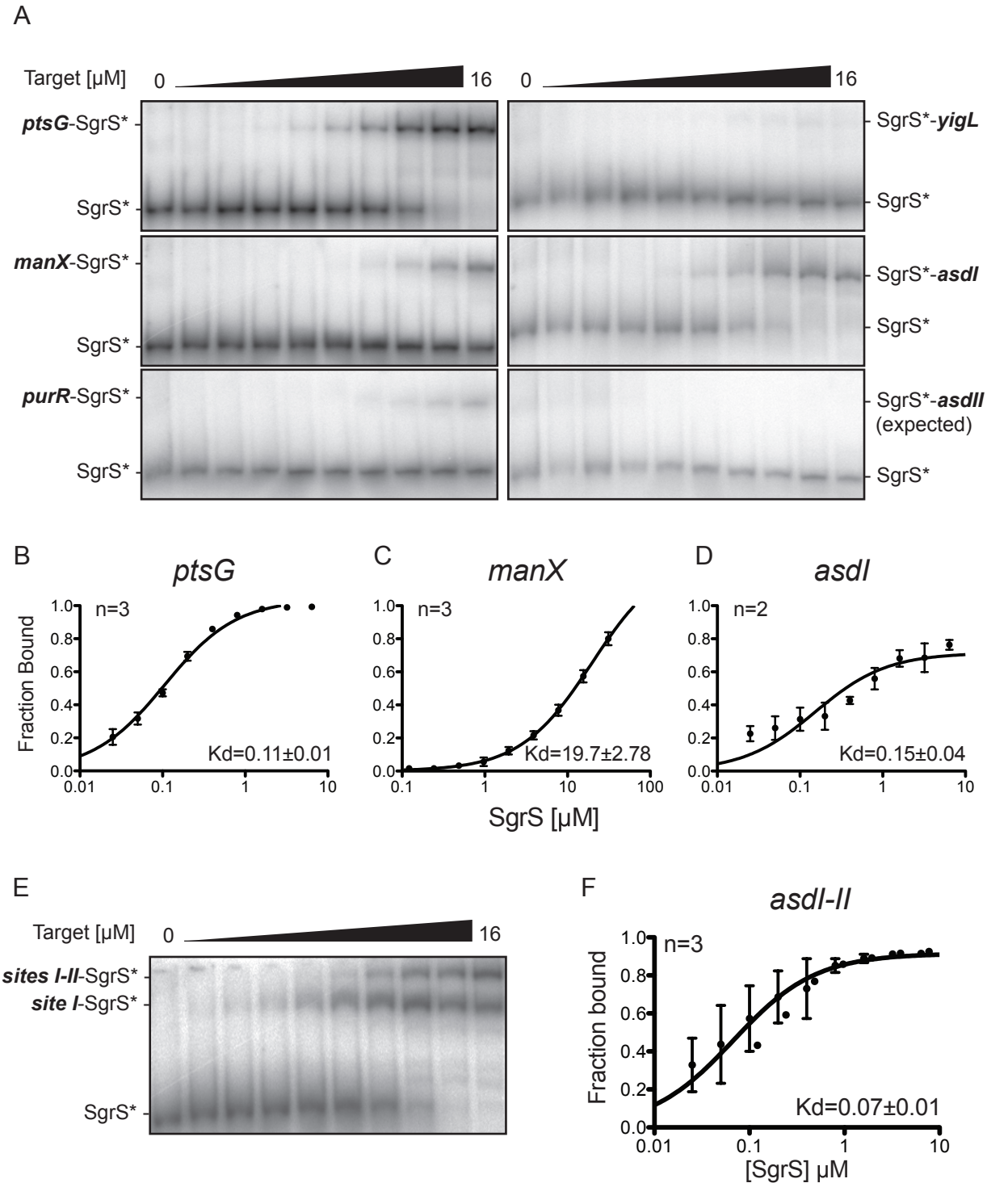

Figure 4 legend on the next page

Figure 4. SgrS binding with target mRNAs *in vitro*. A) SgrS was labeled with ^{32}P and incubated with unlabeled target transcripts at final concentrations of 0μM - 16 μM . Electrophoretic mobility shift assays (EMSAs) were performed after incubating full-length SgrS (+1 to +227) with its target transcripts (A) *ptsG* (+1 to +240), *manX* (+1 to +240), *purR* (+1 to +230), *yigL* (-191 to +50 relative to ATG translation start of *yigL*), *asdI* (+1 to +110), and *asdII* (+71 to +310). B-D) Targets transcripts (B) *ptsG* (+1 to +240), (C) *manX* (+1 to +240), (D) *asdI* (+1 to +110) were labeled with ^{32}P and incubated with unlabeled SgrS. EMSAs were performed to resolve complex formation. Band densities were measured for biological replicates (n, top left) and plotted to determine dissociation constant (K_D, bottom right) values for (B) *ptsG*, (C) *manX*, and (D) *asdI*. E) EMSA of radiolabeled SgrS in the presence of increasing concentrations of *asdI-II* transcript. Shift in mobility corresponding to one or two SgrS bound to *asdI-II* is denoted as Site I-SgrS* and Sites I-II-SgrS* respectively. F) Quantification of SgrS binding with radiolabeled *asdI-II* (+1 to +240), as described above.

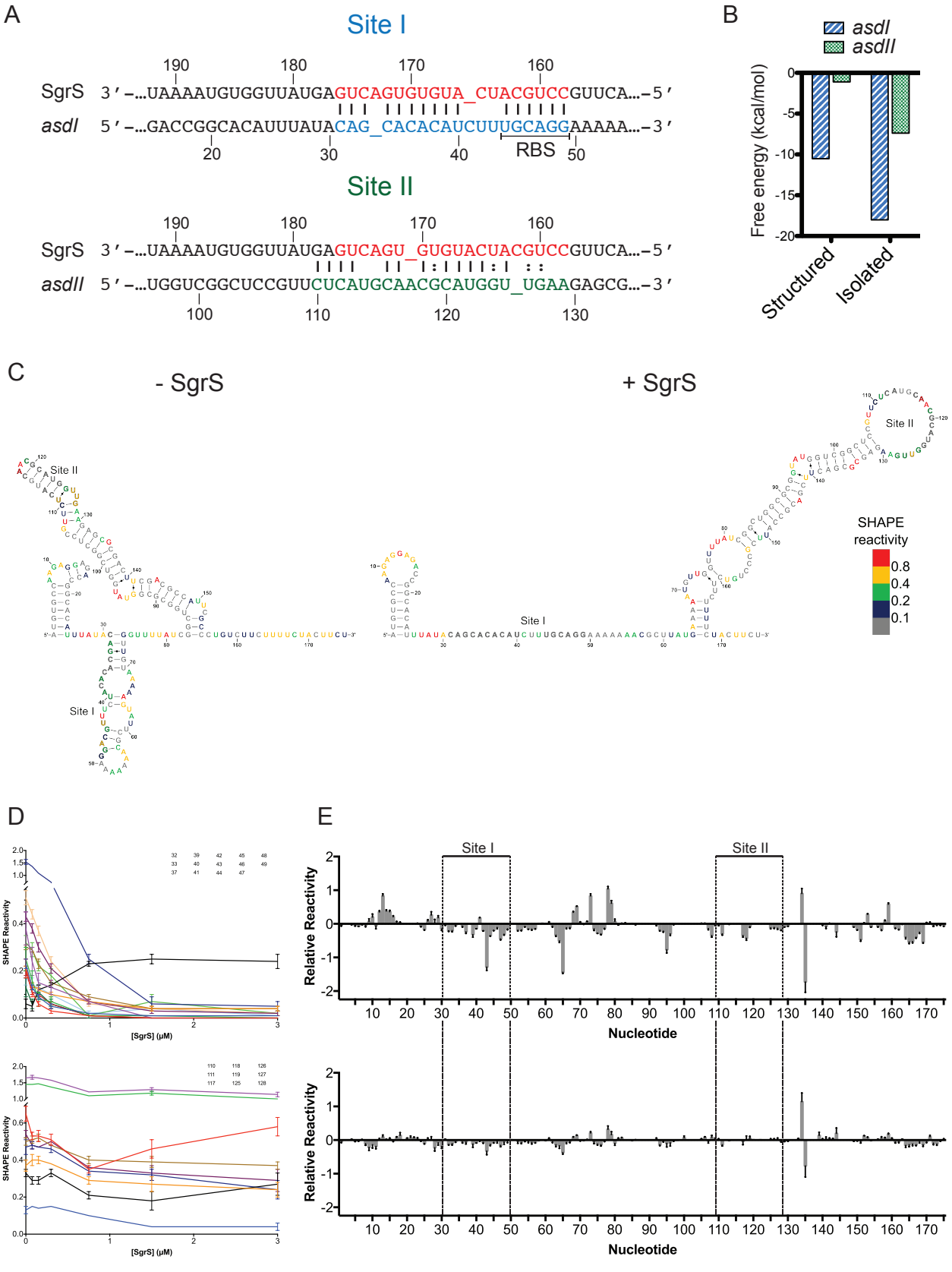

Figure 5 legend on the next page

Figure 5. Secondary structure of 5' end of *asd*. A) Diagram showing base-pairing interactions of SgrS with binding sites I and II of *asd* mRNA. B) Energy of interaction predicted by IntaRNA (26). "Structured" indicates pairing between full length SgrS (+1 to +227) and *asdI-II* (+1 to +180). Plotted is the energy of interactions at either site I (*asdI*) or site II (*asdII*). "Isolated" indicates interactions between isolated binding sites: SgrS (+158 to +176) with *asdI* (+31 to +49) and SgrS (+158 to +178) pairing with *asdII* (+110 to +129). C) The structure of the *asdI-II* RNA alone or in complex with SgrS was probed with NMIA and the modified RNA was analyzed by primer extension inhibition. SHAPE reactivity (difference between the frequency of primer extension products at each nucleotide in +NMIA vs. -NMIA samples) was then used as a parameter in the Vienna RNAprobing WebServer (55) to predict the secondary structure of the *asdI-II* RNA. Colors indicate SHAPE reactivity as following: red, highly reactive (≥ 0.8); gold, reactive (0.4-0.79); green, moderately reactive (0.2-0.39); blue, minimally reactive (0.1-0.19); grey, unreactive (< 0.01). Distinct structures were observed in the absence of SgrS and in the presence of saturating concentrations of SgrS. The SHAPE reactivity of *asdI-II* RNA alone (left) or in the presence of 5-fold excess SgrS (right) is mapped to the predicted secondary structures. (D) SHAPE reactivity as a function of SgrS concentration for each binding site (top, site I; bottom, site II). Only nucleotides with a significant (≥ 0.1) change in reactivity are shown. Error bars denote SEM, n = 9. (E) Relative SHAPE reactivity (difference in the SHAPE reactivity in the presence of SgrS vs. the absence of SgrS) of the *asdI-II* RNA in the presence of wild-type (top) or mutant (bottom) SgrS. Error bars denote SEM, n = 9 (WT), 6 (MT). The *asdI-II* RNA nucleotides are numbered below the X-axis and the SgrS binding sites are indicated.

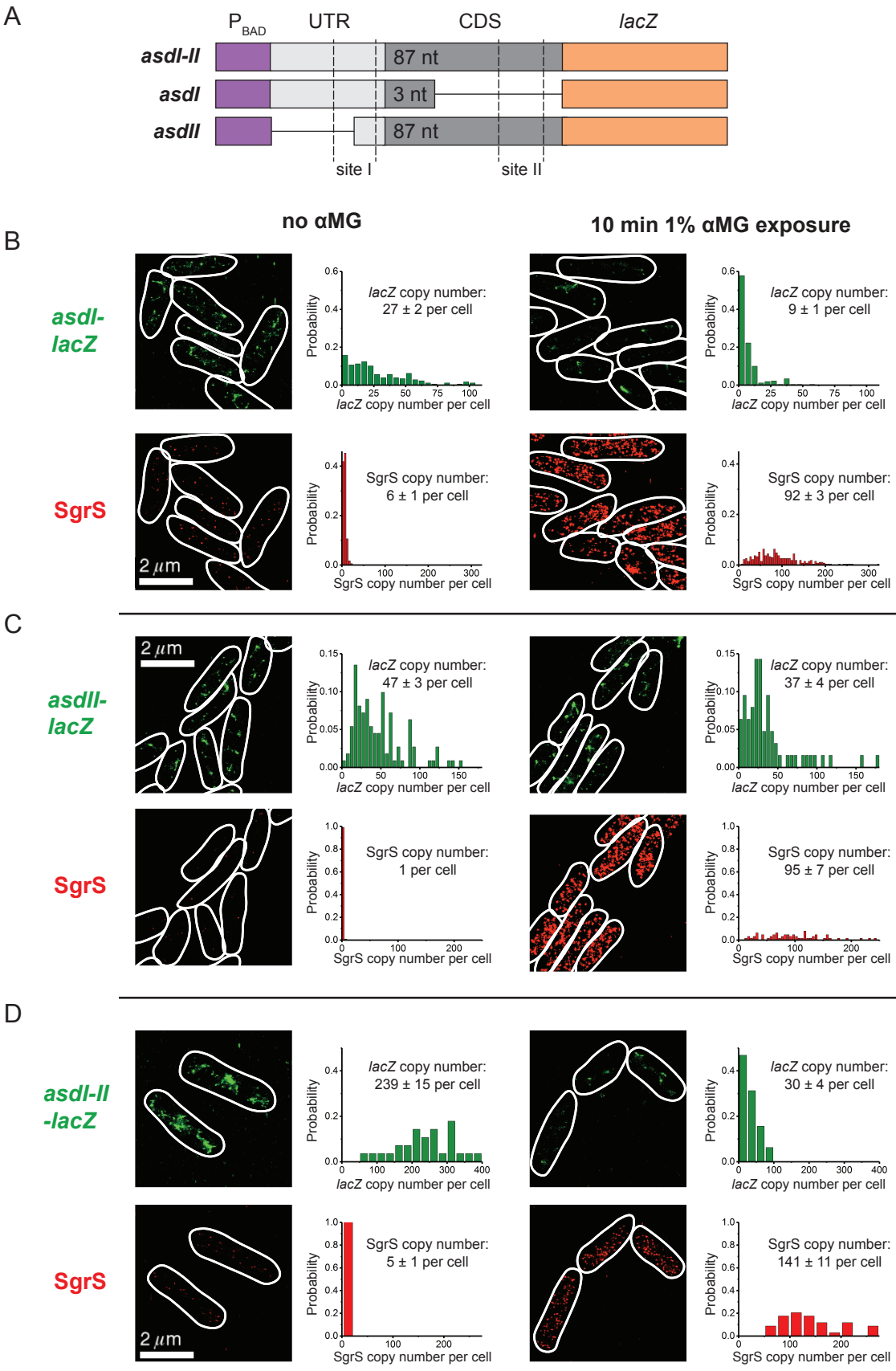

Figure 6 legend on the next page

Figure 6. STORM imaging of SgrS regulation of *asd* variants. A) Illustration of *asdI-II*, *asdI* and *asdII* translationally fused to *lacZ* reporter with SgrS binding sites I and II marked. B-D) 2D projection of 3D super-resolution images of SgrS and *lacZ* mRNA for the different *asd-lacZ* variants, labeled by smFISH, before and after 10 min induction with 1% αMG. (B), (C) and (D) correspond to *asdI-lacZ*, *asdII-lacZ,* and *asdI-II-lacZ* shown in (A). Probability distributions of RNA copy numbers in individual cells for 30-250 cells are plotted next to the representative images.

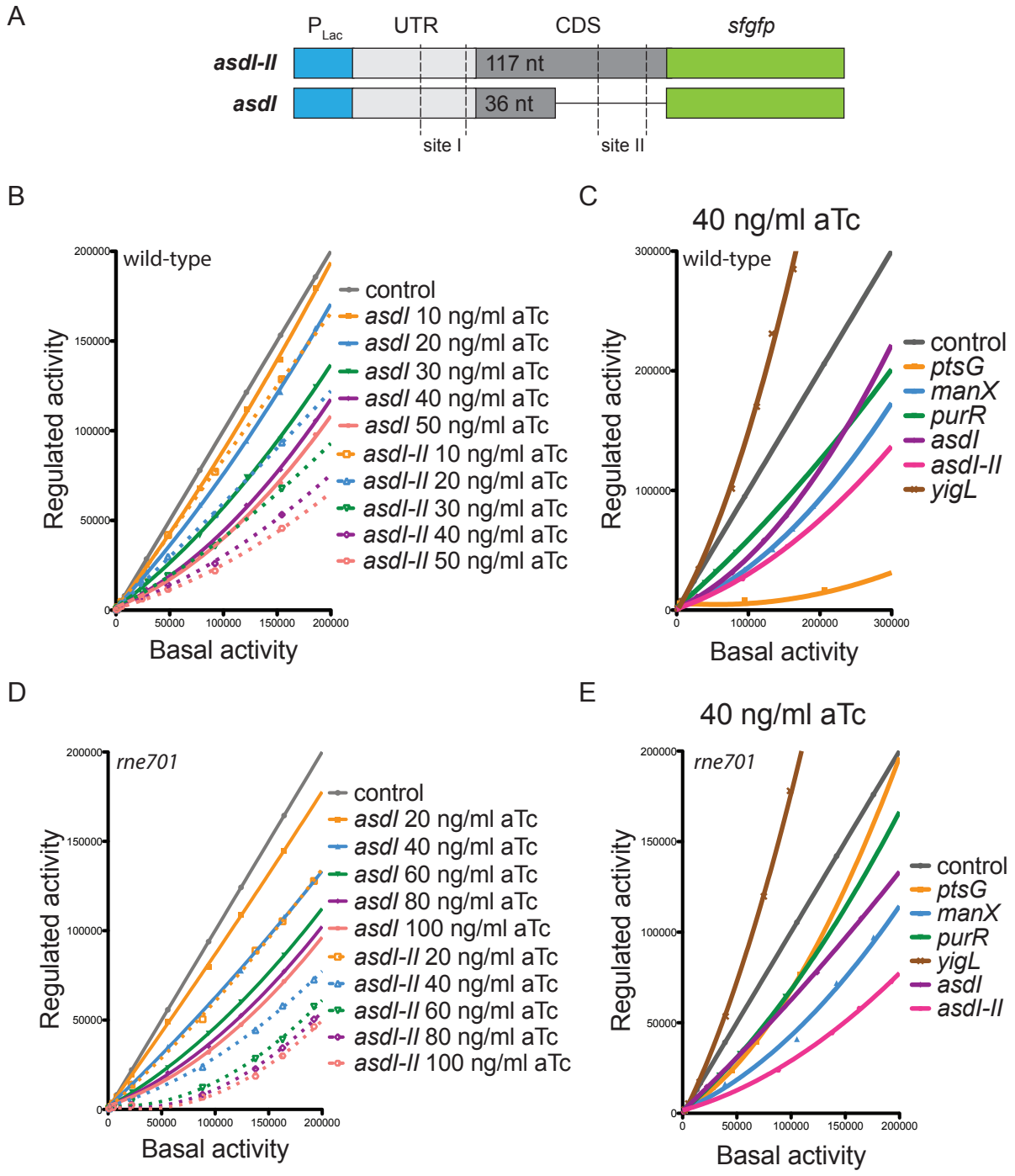

Figure 7. SgrS binding cooperativity allows for improved repression of *asd* translation. A) Illustration of *asdI* and *asdI-II* constructs with SgrS binding sites marked. Graphs show comparison of SgrS regulation of *asdI* and *asdI-II* variants in (B) wild-type and (D) *rne701* mutant by plotting regulated activity over basal activity at various SgrS expression levels (20-100 ng/ml aTc). Regulatory hierarchy of SgrS targets in (C) wild-type and (E) *rne701* mutant strains. Regulation of target genes at one SgrS expression level (40 ng/ml aTc) are compared by plotting regulated activity over basal activity of the *gfp* reporter.

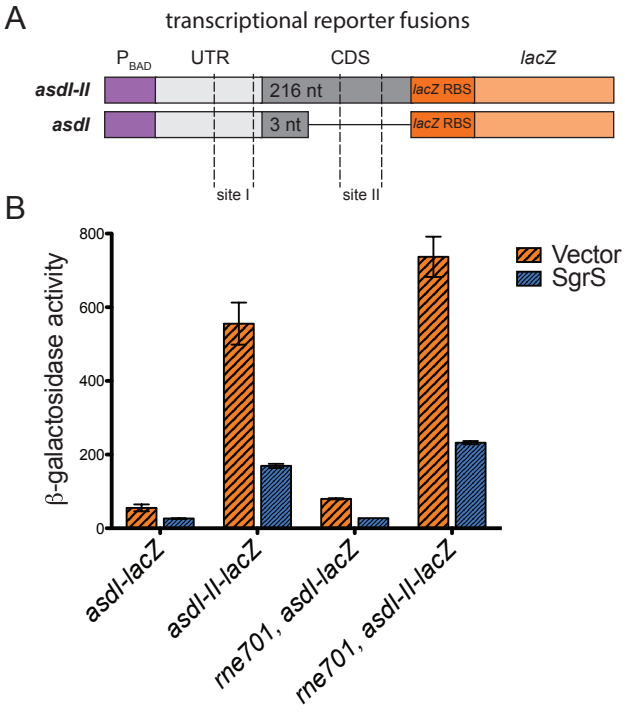

Figure 8. SgrS regulation of transcriptional *asd-lacZ* fusions. β-galactosidase activity of (A) *asdI-lacZ* (+1 to +64) and *asdI-II-lacZ* (+1 to +277) was (B) assayed in response to SgrS expression from a plasmid (and vector control) in WT and *rne701* background strains.